

NANOMATERIALS

Casting inorganic structures with DNA molds

Wei Sun,^{1,2} Etienne Boulais,³ Yera Hakobyan,³ Wei Li Wang,^{1,2} Amy Guan,¹ Mark Bathe,^{3*} Peng Yin^{1,2*}

INTRODUCTION: The ability to manufacture inorganic nanoparticles (NPs) with arbitrarily prescribed three-dimensional (3D) shapes and positional surface modifications is essential to enabling diverse applications (e.g., in nano-optics and bio-sensing). However, it is challenging to achieve 3D arbitrary user-specified shapes with sub-5-nm resolution.

Top-down lithography has limited resolution, particularly for 3D shapes; capping ligands can be used to tune the energy difference of selected crystallographic facets,

but typically only for highly symmetric shapes with identical surface facets.

RATIONALE: We developed a framework to program arbitrary 3D inorganic NPs using DNA, which serves both as an informational “genome” to encode the 3D shape of a NP and as a physical “fabricator” to retrieve the information and execute the instruction to manufacture the NP. Specifically, our method uses a computationally designed, mechanically stiff synthetic DNA nanostructure with a user-specified cavity as a “mold” to cast the target inorganic NP. The mold encloses a small gold (Au) “seed.” Under mild conditions, the Au seed grows into a larger metal

NP that fills the entire cavity, thereby replicating its prescribed 3D shape. The remaining DNA mold additionally acts as a spatially programmable functionalization surface.

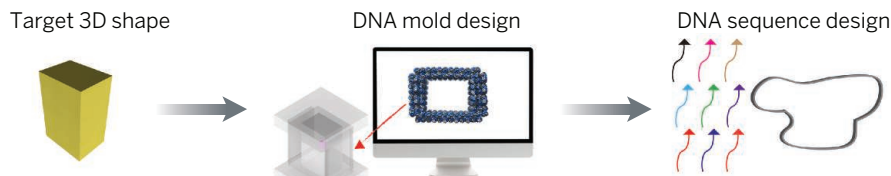
RESULTS: Using this DNA nanocasting method, we constructed three distinct sub-25-nm 3D cuboid silver (Ag) NPs with three independently tunable dimensions. The shape versatility of DNA-based nanocasting was further demonstrated via the synthesis of Ag NPs with equilateral triangular, right triangular, and circular cross sections. The material versatility was demonstrated via synthesis of a Au cuboid in addition to the Ag NPs. The DNA mold served as an addressable coating for the casted NP and thus enabled the construction of higher-order composite structures, including a Y-shaped Ag NP composite and a quantum dot (QD)-Ag-QD sandwiched structure through one-step casting growth.

We investigated the key design parameters for stiff DNA molds through mechanical simulations. Multilayered DNA molds provided higher mechanical stiffness for confining NP growth within the mold than single-layer DNA molds, as confirmed by experimental observation.

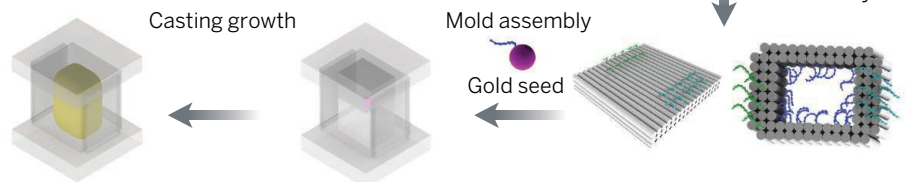
We additionally characterized plasmonic properties of the designer equilateral Ag triangle and Ag sphere through electron energy loss spectroscopy. Tuning of particle symmetry produced a shape-specific spectrum, which is consistent with the predictions of electromagnetism-based simulations.

CONCLUSION: DNA nanocasting represents a new framework for the programmable digital fabrication of 3D inorganic nanostructures with prescribed shapes, dimensions, and surface modifications at sub-5-nm resolution. The key design strategy is to encode linear sequences of DNA with the sophisticated user-specified 3D spatial and surface information of an inorganic NP, as well as to retrieve and execute the information to physically produce this structure via geometric confinement. Such a method may lead to computationally designed functional materials for the digital manufacture of optical nanocircuits, electronic nanocomputers, and perhaps even sophisticated inorganic nanorobots, each with their blueprints (or “genomes”) encoded in the DNA molecules that constitute their “nanofabricators.” ■

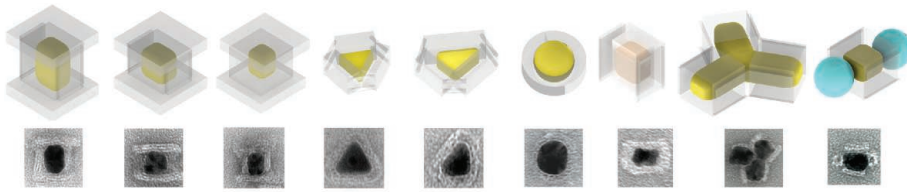
Computational design



Chemical synthesis



Experimental results



Casting metal particles with prescribed 3D shapes using programmable DNA nanostructure molds. (Top): Schematic of computational shape-by-design framework to encode the user-specified 3D shape of an inorganic particle in the linear sequences of DNA. (Middle): Assembly of the mold and casting growth of the metal particle. (Bottom): Experimental characterization of cast products (transmission electron micrographs; scale bars, 20 nm).

¹Wyss Institute for Biologically Inspired Engineering, Harvard University, Boston, MA 02115, USA. ²Department of Systems Biology, Harvard Medical School, Boston, MA 02115, USA. ³Department of Biological Engineering, Massachusetts Institute of Technology, Cambridge, MA 02139, USA. *Corresponding author. E-mail: py@hms.harvard.edu (P.Y.); mark.bathe@mit.edu (M.B.) Cite this article as W. Sun et al., *Science* 346, 1258361 (2014). DOI: 10.1126/science.1258361

RESEARCH ARTICLE

NANOMATERIALS

Casting inorganic structures with DNA molds

Wei Sun,^{1,2} Etienne Boulais,³ Yera Hakobyan,³ Wei Li Wang,^{1,2} Amy Guan,¹ Mark Bathe,^{3*} Peng Yin^{1,2*}

We report a general strategy for designing and synthesizing inorganic nanostructures with arbitrarily prescribed three-dimensional shapes. Computationally designed DNA strands self-assemble into a stiff “nanomold” that contains a user-specified three-dimensional cavity and encloses a nucleating gold “seed.” Under mild conditions, this seed grows into a larger cast structure that fills and thus replicates the cavity. We synthesized a variety of nanoparticles with 3-nanometer resolution: three distinct silver cuboids with three independently tunable dimensions, silver and gold nanoparticles with diverse cross sections, and composite structures with homo- and heterogeneous components. The designer equilateral silver triangular and spherical nanoparticles exhibited plasmonic properties consistent with electromagnetism-based simulations. Our framework is generalizable to more complex geometries and diverse inorganic materials, offering a range of applications in biosensing, photonics, and nanoelectronics.

Synthesis of shape-controlled inorganic structures underlies diverse applications in biosensing (1), light harvesting (2), and nanophotonics (3). Although a wide variety of synthetic nanostructures have been reported, the formation of nanoparticles (NPs) with arbitrarily prescribed three-dimensional (3D) shape and positional surface modification of sub-5-nm resolution has not been demonstrated with inorganic materials. Top-down lithography (e.g., electron beam lithography) has limited resolution, particularly for 3D shapes (1, 4). In addition, it is a slow serial process and is therefore unsuitable for large-scale production. Capping ligands can be used to tune the energy difference of selected crystallographic facets, and hence NP growth dynamics, to produce diverse symmetric shapes (5–11). However, reliable dynamic growth simulation models are typically limited to highly symmetric shapes of identical surface facets (11–14), and it is challenging to predict irregular shapes or to control final NP dimensions.

Structural DNA nanotechnology (15) provides a promising route to overcoming these limitations. Using DNA molecules as construction materials, researchers have rationally designed and synthesized diverse shape-controlled nanostructures (16–28). Building on this success, we have developed a general framework to program 3D inorganic shapes (fig. S1) (29). Our approach uses computationally designed, chemically stable, and mechanically stiff DNA nanostructures as molds to cast metallic NPs of user-specified 3D shape, which

can be asymmetric. A “nanomold” is self-assembled from DNA strands, contains the user-designed 3D cavity, and encloses a small nucleating gold (Au) seed. Under mild conditions, the Au seed grows into a larger metal cast NP that fills the entire cavity of the mold, thereby replicating its 3D shape.

Using this nanocasting method, we constructed three distinct sub-25-nm 3D cuboid silver (Ag) NPs with three independently tunable dimensions. The shape versatility of DNA-based nanocasting was further demonstrated via the synthesis of Ag NPs with equilateral triangular, right-triangular, and circular cross sections. Material versatility was demonstrated via synthesis of a Au cuboid in addition to the Ag NPs. The DNA mold served as an addressable coating for the cast NP and thus enabled the construction of higher-order composite structures, including a Y-shaped Ag NP composite and a quantum-dot (QD)–Ag-QD sandwiched structure. Finally, the designer equilateral Ag triangle and Ag sphere exhibited plasmonic properties that are consistent with electromagnetism-based simulations.

By serving both as an informational “genome” to carry the user-designed blueprint of the inorganic shape in a digitally precise fashion and as a physical “fabricator” for its accurate execution, DNA enables a new kind of shape-by-design framework for inorganic nanostructure fabrication and promises diverse transformative applications. For example, because the plasmonic properties of shape-controlled metal NPs can be predicted quantitatively in silico, the current shape-by-design framework can be further generalized to be a property-by-design framework for producing inorganic nanostructures with prescribed functional properties.

Ag cuboid casting

Figure 1A depicts the process of casting a cuboid-shaped Ag NP. First, we construct a DNA mold

for the casting (steps 1 to 3). In steps 1a and 1b, an open-ended DNA nanostructure barrel and two DNA lids are respectively designed and assembled according to computed stiffness design. In step 2, a 5-nm Au NP is anchored to the interior surface of the barrel. In step 3, the attachment of the two lids to the barrel results in a box-like DNA mold with a cuboid cavity. At the end of step 3, we have constructed a DNA mold with a cuboid cavity and a Au seed inside. With this mold, in step 4 (the casting step), under suitable chemical conditions, the Au seed grows into a Ag NP confined by the mold. Using this strategy and its variants, we fabricated diverse shape-controlled NPs (Fig. 1B). We next describe the design and construction details for casting a Ag cuboid NP using the aforementioned strategy (Fig. 1A).

Computational design of the DNA mold

To design mechanically stiff molds for geometrically constrained metal growth in solution, we used scaffolded DNA origami (22), which enables the precise nanometer-scale design of complex 3D cavities of prescribed mechanical properties. The DNA sequences for the DNA mold were designed using caDNAno software (30), and its mechanical ground-state 3D solution structure and mechanical properties were then predicted by CanDo (31, 32). Briefly, CanDo computes 3D solution structure by modeling B-form DNA as a continuous elastic rod with effective geometric and material properties. Crossovers are assumed to rigidly constrain adjacent helices on a square or honeycomb lattice. Effective mechanical properties of the molds, including their ground-state solution structures and their mechanical deformations in response to loading forces, are computed using the finite-element method (29).

We first designed a multilayer DNA mold with a cuboid cavity. The sidewalls of the DNA mold were designed to possess two or three layers of parallel DNA helices with 12 crossovers per helix on average (Fig. 1A). Two or three layers of sidewall thickness were selected to balance the competing needs to optimize structural stiffness and to increase the cavity dimensions; thicker sidewalls result in higher structural stiffness but smaller cavity size, owing to the length limit of the scaffold strand (8064 nucleotides). The x - y cross section of the central cavity was designed to be eight helices by six helices, with a z -dimensional height of nine helical turns. This provides a designed cuboid cavity (after the lid attachment in step 3) measuring 21 nm by 16 nm by 31 nm, assuming a hydrated helix width of 2.6 nm and a helical turn length of 3.4 nm (33). Simulation by CanDo verified that the ground-state solution structure of the DNA mold adopted the cuboid shape cavity (Fig. 2A and fig. S4A). We additionally examined the structural integrity of the mold using normal mode analysis (29).

To effectively confine metal growth, it is important that the DNA mold be sufficiently stiff. We therefore studied its response to different loading forces along the x and y directions (Fig. 2, B and C). The ground-state structure of the cuboid mold was used as the initial configuration

¹Wyss Institute for Biologically Inspired Engineering, Harvard University, Boston, MA 02115, USA. ²Department of Systems Biology, Harvard Medical School, Boston, MA 02115, USA.

³Department of Biological Engineering, Massachusetts Institute of Technology, Cambridge, MA 02139, USA.

*Corresponding author. E-mail: py@hms.harvard.edu (P.Y.); mark.bathe@mit.edu (M.B.)

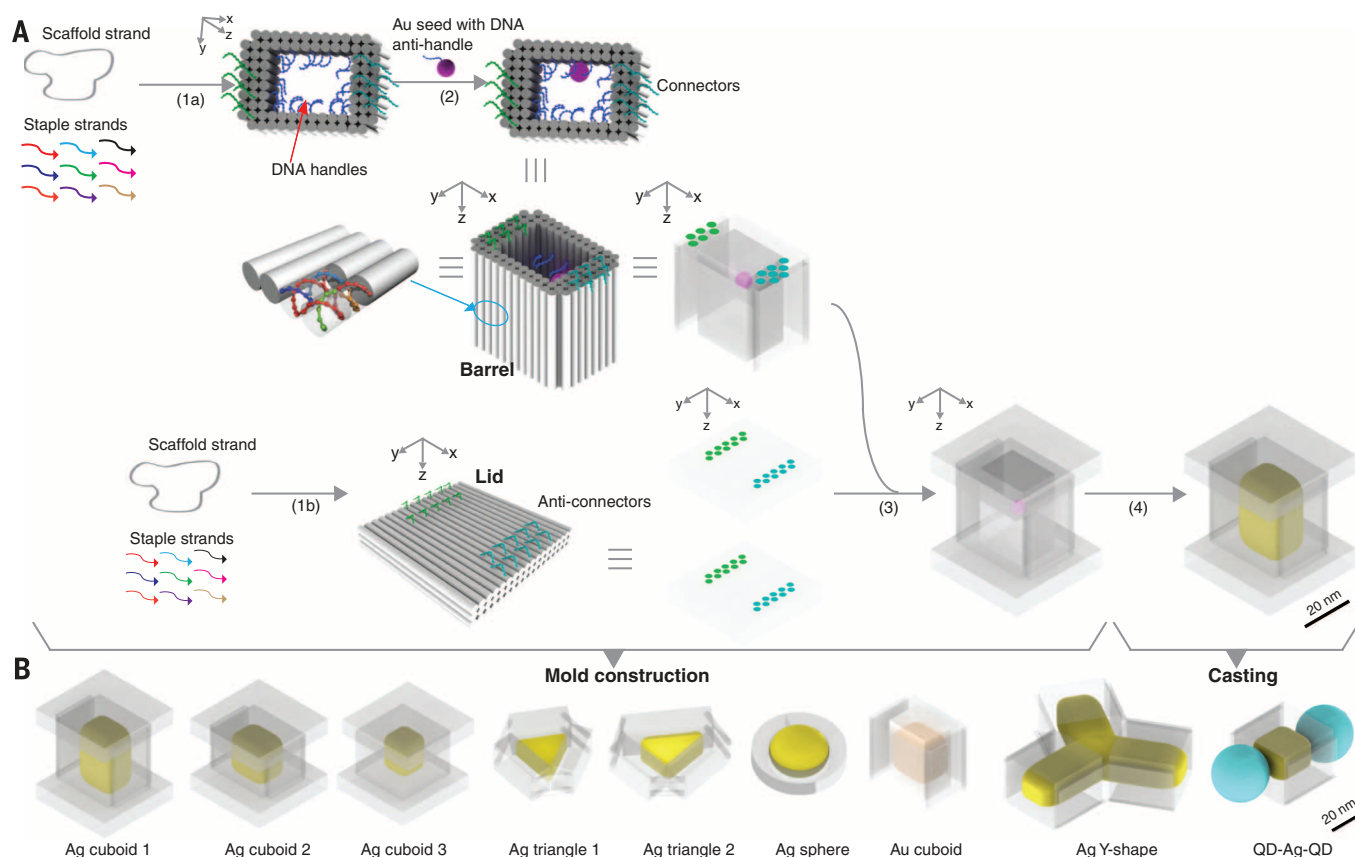


Fig. 1. Casting metal NPs with prescribed shapes using DNA nanostructure molds. (A) Design schematic for casting of Ag cuboid. Cyan and green dots denote (anti-)connectors. (B) Silver (yellow color) and gold (orange color) NPs cast within DNA molds (transparent layer). Ag, silver; Au, gold; QD, quantum dot (depicted as a cyan ball).

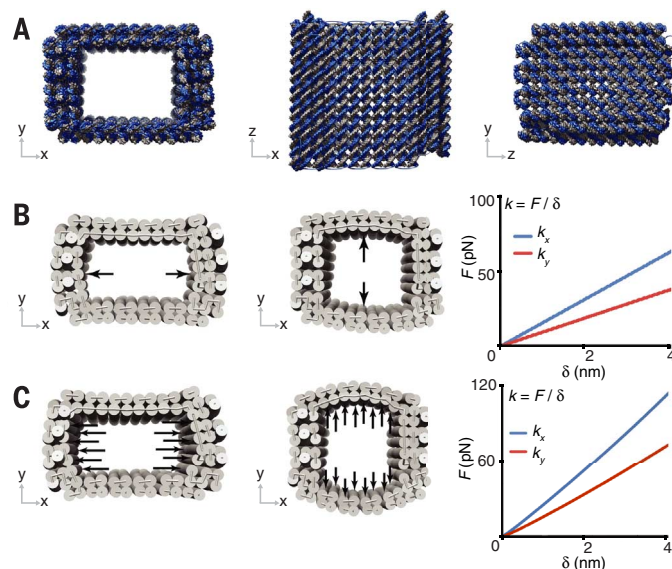
to which two types of loading were applied to model distinct types of mechanical inhibition from the mold onto a given growing NP, namely point contact (fig. S2) or distributed contact (fig. S3). In the point-contact model, a growing NP is assumed to contact a single pair of directly opposing points of the mold (Fig. 2B and table S1, top); equal and opposite point forces are applied to the mold and its deformation is computed. In the distributed-contact model, a growing NP is assumed to fully fill the mold cavity so that the NP applies a uniformly distributed force along opposing interior walls of the cavity (Fig. 2C and table S1, bottom). Under the point-contact scenario, the force response for the barrel was 17 pN/nm in the x direction, normal to the three-layer wall, and 10 pN/nm in the y direction, normal to the two-layer wall. In comparison, higher force-response values were found for the distributed-contact scenario, around 30 pN/nm in the x direction, normal to the three-layer wall, and 19 pN/nm in the y direction, normal to the two-layered wall.

The simulated mechanical properties of the DNA mold (i.e., threshold force and linear deformation range) were found to be comparable to those of viral capsids (34), which have been used to effectively confine inorganic nanomaterials grown within (35) [see (29) for calculation and comparison details]. This result suggests that the DNA mold is also sufficiently stiff to confine

Fig. 2. Mechanical simulations of the rectangular DNA mold.

(A) Ground-state solution conformation predicted for DNA mold with a cuboid cavity, 21 nm by 16 nm by 30 nm.

(B and C) Under point-contact loading (B) and distributed-contact loading (C), the force-deformation (F - δ) response in the x and y directions for the DNA mold in (A); k is the predicted stiffness value along the direction specified.



metal NP growth within, although growth expansion forces can produce slightly increased [up to 20% according to simulation (29)] mold dimensions through elastic deformation of double-stranded DNAs. Notably, mold stiffness was affected by the sidewall thickness. Mechanical simulation revealed that the force response value

increased by a factor of 7 from one to three layers under the point-contact loading scenario (see tables S1, S4, and S5).

Design details

The above computation suggests that our designed DNA mold (i) has the expected ground-state

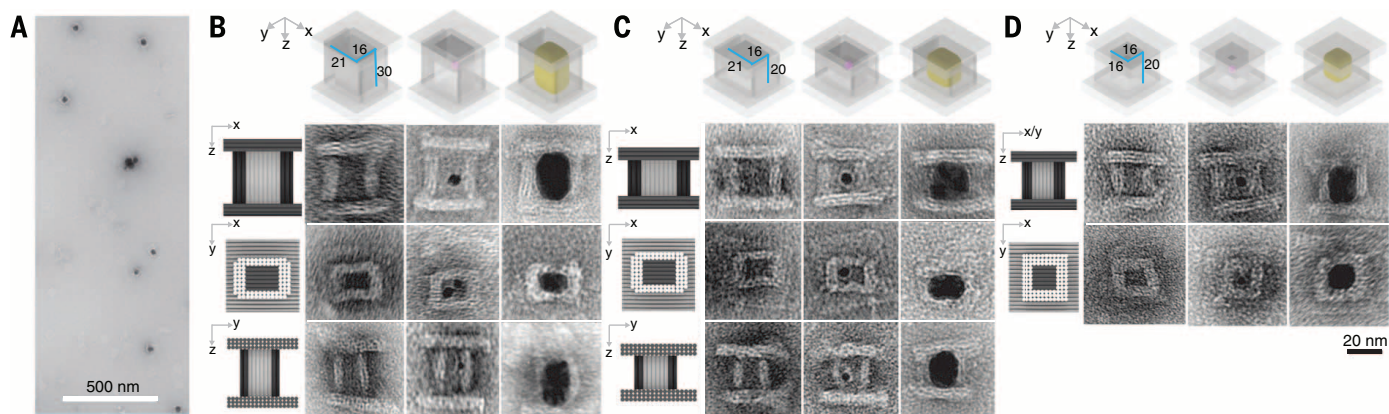


Fig. 3. Casting Ag cuboids with prescribed dimensions. (A) A large view TEM image for the Ag NP grown within the DNA mold with a 21 nm by 16 nm by 30 nm (or 21-16-30 nm) cuboid cavity [as shown in (B)]. (B to D) Design (top row) and TEM images (rows 2 to 4) of the Ag NPs grown in the DNA molds with dimensions of 21-16-30 nm (B), 21-16-20 nm (C), and 16-16-20 nm (D). In row 1 of each panel, small purple dot represents Au seed; cast Ag NP is shown in yellow. In rows 2 to 4 of each panel, a projection model is presented to the left of the TEM images. TEM images from left to right: empty DNA box, DNA box decorated with Au seed (small dark dots; see also figs. S47 to S49), and DNA box containing fully grown Ag NP (dark rectangles with rounded corners; see also figs. S52 to S54).

Table 1. Casting yield for different shaped NPs.

Casting yield refers to NP growth yield in step 4 (Fig. 1) and was calculated as the ratio between the number of DNA molds with metal NPs of designed shapes and dimensions and the total number of seed-decorated DNA molds. See text and (29) for details. See table S6 for the yields of each step in constructing the seed-decorated molds, which are not accounted for in calculating the casting yield.

Shape	Casting yield (step 4)
Ag cuboid 1	40%
Ag cuboid 2	33%
Ag cuboid 3	39%
Ag triangle 1	10%
Ag triangle 2	14%
Ag sphere	18%
Au cuboid 1	6%
Ag Y-shape	10%
QD-Ag-QD	31%

solution conformation, and (ii) has sufficient mechanical stiffness to confine metal NP growth. Thus, we used this design for step 1a. In step 1b, a three-layered DNA lid was designed with 18 helices in the y direction, three helices in the z direction, and 13 helical turns in the x direction (Fig. 1A).

In step 2, for attachment of the Au “seed” to the DNA barrel (36), 27 single-stranded DNA (ssDNA) “handles,” each 21 nucleotides (nt) in length, were immobilized in the interior surface of the barrel (Fig. 1A). A 21-nt “anti-handle” (an ssDNA with sequence complementary to the handle) was immobilized onto the Au seed surface. The stoichiometric ratio between the anti-handle and the Au seed was set at 1:1 to achieve approximately one anti-handle per seed, based on a previous report (37). The hybridization between the handle and the anti-handle anchored the Au seed to the interior of the barrel. Au was favored over Ag for the choice of seed because of the stability and nucleation versatility of Au (38–41).

To assemble the seed-decorated barrel and the lids in step 3, the barrel was designed to carry 14 and 16 ssDNA “connectors,” each 16 nt in length, on both ends (fig. S28, left), and one side of the lid was designed to carry 20 complementary “anti-connectors.” Connectors and anti-connectors were designed to be positioned in roughly matching patterns. Hybridization between them brought the barrel and the two lids together, completing the assembly of a box-like mold with a fully enclosed cuboid cavity. The ~ 0.5 -nm gap between neighboring DNA helices (not depicted in the figure) that constituted the mold was expected to permit the diffusion of small ions or molecules, such as metal ions and ascorbic acid, into the enclosed box. In step 4, under suitable chemical conditions (see below), the Au seed would grow into a Ag cuboid that filled the cavity.

Experimental implementation

In a typical experiment, DNA barrels and lids were folded separately by slowly annealing the staple/scaffold mixtures from 80°C to 24°C over 72 hours. Crude products were subjected to 1.5% agarose gel electrophoresis with 0.5× TBE/10 mM Mg(NO₃)₂ as running buffer. Purified structures were extracted and subsequently recovered via centrifugation. Seed decoration was executed by incubating DNA barrels with 5-nm Au NPs (at a seed-to-barrel stoichiometry ratio of 2:1) at 35°C for 16 hours and then annealed to 24°C over 3 hours. Excess Au seeds were removed with a size-exclusion spin column. DNA lids were mixed with the seed-decorated DNA barrels (at lid-to-barrel stoichiometry ratio of 3:1) at 35°C for 16 hours and annealed to 24°C over 3 hours. Growth of Ag NPs in step 4 was triggered by the addition of silver nitrate (1.4 mM) and ascorbic acid (2 mM). After growth for 10 min at room temperature in dark conditions, Ag NPs grown within DNA boxes were imaged by transmission electron microscopy (TEM). See (29) for experimental details of mold assembly and purification, metal growth, and TEM sample preparations.

TEM characterization

TEM imaging confirmed successful formation of barrels in step 1a (fig. S23), formation of the lids in step 1b (fig. S30), attachment of Au seed to the barrel in step 2 (fig. S39), assembly of lids with the seed-decorated barrel in step 3 (Fig. 3B, middle, and fig. S47), and finally formation of Ag cuboids with expected dimensions in step 4 (Fig. 3A, Fig. 3B, right, and fig. S52). In a supporting experiment, lids also assembled successfully with a seed-free barrel (Fig. 3B, left).

From three projectional views of the TEM images (Fig. 3B, left column), the x - y , x - z , and y - z dimensions of the barrel cavity were measured respectively as 19.3 ± 1.5 nm by 13.3 ± 0.4 nm, 19.3 ± 1.5 nm by 30.5 ± 1.0 nm, and 13.3 ± 0.4 nm by 30.5 ± 1.0 nm ($N = 20$ for each projectional view), each approximately consistent with the designed 21 nm by 16 nm by 30 nm cuboid cavity enclosed in the box. From the x - y projection TEM image (Fig. 3B, middle row), the thicknesses of the top and bottom sidewalls of the barrel were measured to be 5.6 ± 0.2 nm ($N = 20$) and the left and right sidewalls were measured to be 7.8 ± 0.1 nm ($N = 20$); similar measurements were also obtained from x - z and y - z projections), which were in approximate agreement with two- or three-layered designs. However, because of partial dehydration and structural deformation during TEM sample preparation, small deviations of 2 to 3 nm were occasionally observed in some structures. The DNA lid exhibited the designed 39.5 ± 2.6 nm by 47.7 ± 0.7 nm ($N = 20$) dimensions under TEM (fig. S30). Because the barrel was designed to carry 27 handles, multiple seeds could in principle be attached to the barrel; here, we experimentally observed one to five seeds present in a single barrel (Fig. 3B, middle, and fig. S39).

After growth, the seed turned into a Ag cuboid, as revealed by the TEM images of dark rectangular projections in the x - z , x - y , and y - z planes, with an expected length of 21.2 ± 0.7 nm by 16.0 ± 0.4 nm by 32.1 ± 1.4 nm in x - y - z dimensions ($N = 20$ for each projectional view; Fig. 3A, Fig. 3B,

right, and figs. S51 and S52). Measured dimensions of the NP were slightly larger than the measured dimensions of the cavity, suggesting compression of the DNA mold sidewalls by the Ag NP growth. The presence of 4- to 8-nm-thick sidewalls (light-colored) around the NP (dark-colored) in the TEM images suggests that the DNA mold remained surrounding the NP after growth. Notably, all the Ag cuboids grown within the DNA molds exhibited round rather than sharp corners, in the absence of surface capping ligands. Such rounded corners are likely a consequence of surface energy minimization of Ag NPs by decreasing the number of dangling bonds at NP corners. In a supporting experiment, we removed one or two lids from the DNA box, and observed that some Ag NPs grew out of the DNA barrel (fig. S50). These unconfined Ag NPs exhibited much larger dimensions than those within the DNA barrels, further confirming the designed confinement effect of DNA molds. We observed NP growth only within the mold, not on its exterior surface, confirming the effectiveness of seed-nucleated growth.

Casting yield

Casting yield (40%, Table 1) from step 4 was defined as the ratio between the number of NPs with designed projectional shapes and the total number of seed-decorated boxes (with both lids well attached) in the TEM image (29) (fig. S51). Additionally, the reaction yields for each step in constructing a DNA mold in Fig. 1A are defined in (29) and listed in table S6. Specifically, the barrel formation yield (20%) from step 1a (Fig. 1) was determined from agarose gel (fig. S22) and was measured as the ratio between the molar quantity of the target structure (determined by comparing the SYBR Safe stained target band intensity and the intensity of a standard DNA marker with known molar quantity) and the molar quantity of the initial scaffold strand used in the experiment (29). Lid formation yield (12%) of step 1b was similarly defined and measured (fig. S29). Seed decoration yield (86%) from step 2 was determined as the ratio of the number of barrels with at least one seed attached to the interior surface and the total number of seed-decorated barrels in the TEM image (29). Box closure yield (31%) from step 3 was measured as the ratio of the number of seed-decorated barrels with both lids well attached and the total number of seed-decorated barrels in the TEM image (29).

Tuning the dimensions of the Ag cuboids

The dimensions of the Ag cuboid can be modified by changing the cavity size of the DNA mold. Using this strategy, we tested two additional barrels of different dimensions (figs. S5, S6, S25, and S27 and tables S2 and S3) and assembled DNA boxes accordingly. First, we reduced the z -direction length of the DNA box mold from 30 nm (nine DNA helical turns) to 20 nm (six DNA helical turns), and thus obtained a box with a 19.0 ± 1.4 nm by 13.9 ± 0.3 nm by 22.0 ± 0.9 nm cuboid cavity ($N = 20$ for each projectional view; Fig. 3C, left). After successful seed decoration (see fig. S40), box closure (Fig. 3C, middle, and

fig. S48), and growth, a cuboid with measured dimensions of 20.6 ± 0.7 nm by 16.8 ± 0.7 nm by 21.6 ± 0.9 nm was formed ($N = 20$ for each projectional view; Fig. 3C, right, and fig. S53).

We next further reduced the x dimension from 21 nm (eight helices) to 16 nm (six helices) and obtained a box with a 13.6 ± 0.1 nm by 13.6 ± 0.1 nm by 22.2 ± 0.7 nm cuboid cavity ($N = 20$ for each projectional view; Fig. 3D, left). After seed decoration (fig. S41), box closure (Fig. 3D, middle, and fig. S49) and growth, the cuboid appeared under TEM with a 14.9 ± 1.5 nm by 14.9 ± 1.5 nm square in xy projection ($N = 20$ for each projectional view; Fig. 3D, right and middle), and 14.9 ± 1.5 nm by 22.4 ± 0.7 nm rectangular shapes for xz and yz projections ($N = 20$ for each projectional view; Fig. 3D, right and top, and fig. S54). See Table 1 for casting yield (33 to 39%) and table S6 for yields of different steps in constructing the mold. For each DNA box design, the barrel formation yield (5 to 13%) (figs. S24 and S26), lid formation yield (12%), seed decoration yield (74 to 91%), box closure yield (13 to 21%), and casting yield (33 to 39%) (table S6) (29) were determined following the same definition described above.

NPs with prescribed cross sections

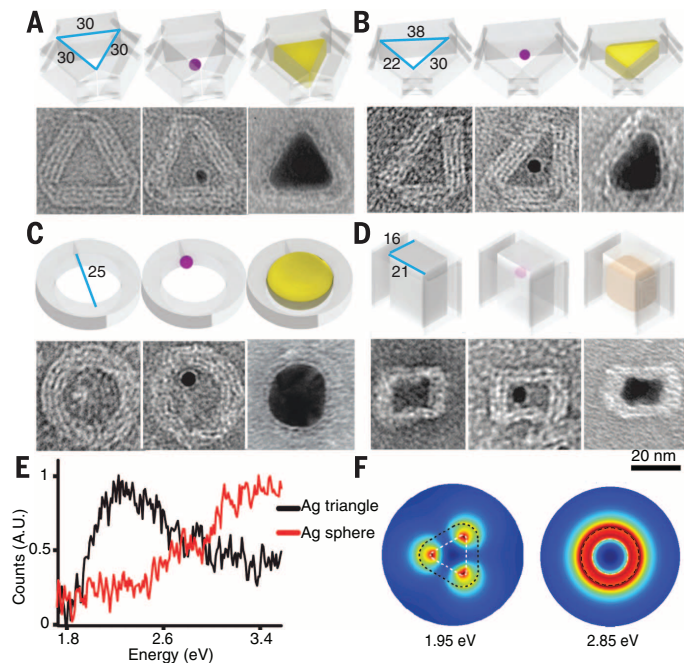
Using a simplified design strategy, we cast Ag NPs with prescribed cross section shapes (without height control). Here, we used open-ended barrel molds containing tunnels with designed shapes. The barrels were designed to have four-layered sidewalls and featured three distinct

cross section cavities: an equilateral triangular channel (Fig. 4A and fig. S32), a right-triangular channel (Fig. 4B and fig. S34), and a circular shape channel (Fig. 4C and fig. S36). For capture of Au seeds, each barrel was designed to display three 21-nt ssDNA handles on its interior surface.

In the equilateral triangular barrel, the cross section of a fully confined Ag NP exhibited an equilateral triangular shape under TEM, with an expected edge length of 25.2 ± 1.9 nm ($N = 20$) and three rounded corners (Fig. 4A, right, and fig. S56). The DNA mold remained intact after Ag growth and wrapped around the Ag NP. No obvious bending or curvature of DNA sidewalls was observed. In the center of the Ag NP, a circular shade with 5-nm diameter was observed and was assigned to the Au seed in the DNA mold. TEM imaging of a tilted conformation further confirmed the 3D nature of the NP (fig. S57A). High-resolution TEM plus electron diffraction characterization (fig. S57, B and C) also revealed the highly crystalline nature of the Ag NP, which was consistent with its smooth surface morphology (absence of grain boundaries) and single seed-mediated growth pathway. In the right-triangular barrel with a measured 21.9 ± 1.1 nm by 30.2 ± 0.5 nm by 37.9 ± 0.5 nm cavity ($N = 20$), the fully grown Ag NP demonstrated a triangular cross section shape with dimensions of 21.7 ± 0.6 nm by 24.2 ± 0.7 nm by 28.2 ± 0.7 nm ($N = 20$; Fig. 4B, right, and fig. S58). Similar to the equilateral triangular NP, the right-triangular NP also exhibited rounded corners. In the circular-shaped channel, a Ag sphere

Fig. 4. Casting Ag and Au NPs with prescribed cross section shapes. In (A) to (D), the top row shows the design and the bottom row shows the TEM images of the empty barrel (left), the seed-decorated barrel (middle), and the fully grown NP (right). In the top row of each panel, the small purple dot represents a Au seed, cast Ag NP is shown in yellow, and Au NP is shown in orange.

(A) Ag NP with 25-nm equilateral triangular cross section (see also figs. S32, S42, and S56). (B) Ag NP with 22-24-28 nm right-angle triangular cross section (see also figs. S34, S43, and S58). (C) Ag NP with 25-nm-diameter circular cross section (see also figs. S36, S44, and S59). (D) Au NP with 19 nm by 14 nm rectangular cross section (see also figs. S23, S39, and S61). (E) EELS measurement for Ag NP with 25-nm equilateral triangular cross section [black, as in (A)] and Ag sphere with 25-nm-diameter circular cross section [red, as in (C)]. (F) Simulated EELS amplitude map for dipolar resonant modes for Ag NP with 25-nm equilateral triangular cross section [as in (A), left] and Ag NP with 25-nm-diameter circular cross section [as in (C), right]. Colors represent simulated amplitude; white and black dashed lines show contours of NP and DNA mold, respectively.



NP was observed with a circular cross section diameter of 25.5 ± 1.6 nm ($N = 20$; Fig. 4C, right, and figs. S59 and S60), consistent with our design. In contrast to the capping ligand method, DNA-based nanocasting enabled one-pot parallel production of distinct prescribed shapes by mixing different molds in a single reaction solution (fig. S65).

In the open barrels, only NPs growing laterally rather than vertically were confined to form-specific shapes. This resulted in NP casting yields of 10 to 18% (Table 1), which is lower than that of the fully enclosed cavity. Most of the unconfined NPs exhibited spherical shapes, and did not fully occupy the channels (figs. S55, S56, S58, and S59; see Table 1 for casting yield and table S6 for yields of different steps in constructing the mold). For each design of open-ended DNA molds, the barrel formation yield (5 to 10%) (figs. S31, S33, and S35), seed decoration yield (60 to 75%), and casting yield (10 to 18%) (table S6) (29) were determined following the same definition described above.

Experimental characterization and simulation of plasmonic properties

Next, we used electron energy loss spectroscopy (EELS) (42) and electromagnetism-based simulations (29) to characterize NP plasmonic behavior, both experimentally and theoretically, of the equilateral Ag triangle in Fig. 4A and the Ag sphere in Fig. 4C.

For the equilateral Ag triangle, EELS measurement (Fig. 4E) showed an intense peak around 2.30 eV (corresponding to 540 nm) with a wide shoulder peak around 3.26 eV (corresponding to 380 nm). Simulation for the same equilateral Ag triangle (figs. S7 and S8) revealed, in the presence of the DNA mold and carbon film beneath, a strong dipolar mode around 1.95 eV from the plasmonic resonance near the corners (Fig. 4F), various resonance modes between 2.45 eV (corresponding to 506 nm) and 3.70 eV (corresponding to 336 nm) near the center and edges, and a bulk Ag plasmon mode at 3.80 eV (corresponding to 327 nm; fig. S9). The red-shifting of the simulated EELS spectra with respect to experiment may be

due to variations in the carbon film thickness of the TEM grid, the dielectric function of the DNA mold, the NP thickness, and the radii of the rounded NP corners (figs. S10 and S11) (29). Simulation of optical properties of the NPs in an aqueous environment indicated plasmonic properties similar to those in vacuum (figs. S16 to S21) (29), suggesting the potential utility of the NPs for biosensing applications. Comparison with a previously published EELS result for a triangular Ag NP of similar dimensions (43) indicates a relative offset of ~ 0.1 eV for the predicted NP dipolar mode resonance, which may be due to the distinct substrate (mica) and surface coating used. In contrast, a larger energy offset of 0.4 eV is observed relative to a previously examined larger equilateral Ag triangle with edge length of 78 nm (43), indicating the importance of NP size on the resonance energy.

A highly distinct EELS response was measured for the Ag sphere (Fig. 4E), indicating shape-specific plasmonic properties. A single resonance band was observed near 3.26 eV (corresponding to 380 nm) experimentally, which was ascribed to the simulated (fig. S12) dipolar mode near 2.85 eV (corresponding to 435 nm; Fig. 4F) at the edge of the NP. Simulations also suggested several minor resonance modes between the 3.30 eV (corresponding to 376 nm) and 3.65 eV (corresponding to 340 nm) regions near the center of the NP (fig. S13). Similar environmentally sensitive resonance was also observed for the cast Ag sphere (figs. S14 and S15).

Further high-resolution EELS characterization or polarized light excitation using dark-field microscopy on the surface-immobilized metal NPs should reveal the spatial distribution of excited surface plasmons (43, 44), which could enrich our fundamental understanding of nano-optics.

Au cuboid casting

To test the material versatility of our strategy, we cast a Au NP in a DNA barrel containing a 16 nm by 21 nm rectangular open tunnel. Relative to the Ag NP, the growth kinetics of the Au NP in $0.5 \times$ TBE/10 mM $\text{Mg}(\text{NO}_3)_2$ buffer was much slower.

After 30 min of reaction time, no obvious size increase was observed for the NP, which was ascribed to the chelating effect of EDTA on gold precursors. Removing EDTA from the reaction buffer promoted the growth kinetics, where a reaction time of 30 min generated a Au NP with a 13.5 ± 0.7 nm by 19.0 ± 1.8 nm ($N = 20$) rectangular cross section within the barrel (Fig. 4D, right, and fig. S61). The casting yield (6%; table S6) was determined following the same definition described above. See (29) for yields of each step.

Composite structures

In addition to structural confinement and protection against undesired NP aggregation, the DNA mold provides a uniquely addressable 3D coating for the NP to be cast, which facilitates the composition of the DNA molds into higher-order complex structures. Here, we experimentally constructed a Y-shape Ag NP branched structure and a QD-Ag-QD composite structure.

A Y-shape DNA mold was assembled from three DNA barrels carrying complementary connector strands (fig. S37). Each barrel carried ssDNA handles to capture Au seeds. After seed decoration, TEM images revealed formation of the desired trimer (Fig. 5A, center, and fig. S45), as well as unintended by-products, such as incompletely assembled dimers and multimers (e.g., pentamers and hexamers). Ag growth within the Y-shape barrel complex generated individual NPs within each barrel, which together formed a Y-shape NP cluster (Fig. 5A, right, and fig. S62). The measured widths of Ag NP within each barrel were 22.7 ± 1.8 nm, 24.3 ± 1.4 nm, and 25.5 ± 0.9 nm ($N = 20$), slightly larger than the designed 21-nm width of the barrel mold. At the center of the Y-shape barrel complex, where the growth fronts of the Ag NPs met, narrow (< 2 nm) interparticle gaps were observed. The casting yield (10%; table S6) was determined following the same definition described above. See (29) for yields of each step.

To build a composite structure where a Ag NP was sandwiched between two QDs, 5 or 6 biotin groups were introduced at both ends of a DNA barrel with a 21 nm by 16 nm by 30 nm cuboid

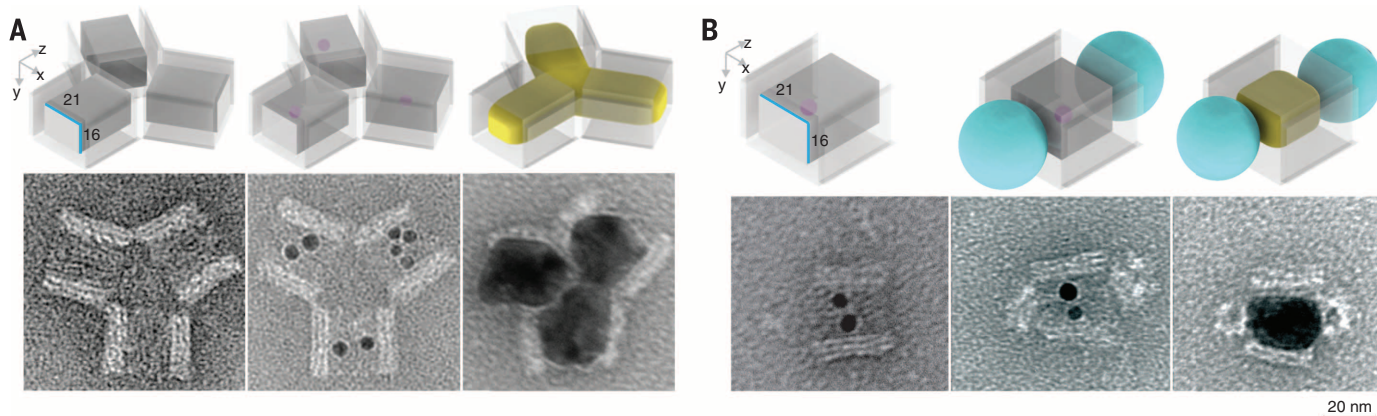


Fig. 5. Casting composite structures. (A) Y-shaped Ag NP junction. Top, schematics; bottom, TEM images of Y-shaped DNA barrel trimer (left), with seed decoration (middle), and Ag NP grown within (right) (see also figs. S45 and S62). (B) QD-Ag-QD composite structure. Top, schematics; bottom, TEM images of DNA barrel with seed decoration (left), QD attached (middle), and Ag NP grown within (right). Small purple dot represents Au seed; cast Ag NP is shown in yellow. The streptavidin-PEG layer of the QD is depicted as a cyan ball (see also figs. S46 and S63).

tunnel (fig. S38). After attaching a Au seed inside the barrel, streptavidin-coated QDs were introduced and bound to both ends of the barrel. TEM imaging revealed the formation of the designed sandwiched structure between QDs and the seed-decorated barrels (Fig. 5B, middle, and fig. S46). After staining with uranium salt (29), the white sphere with 16- to 21-nm diameter at the ends of the barrel was attributed to the polyethylene glycol (PEG) and streptavidin coating layer around QD cores (CdSe@ZnS; see fig. S64 for control experiments with QD only). The conjugation yield of QDs to both ends of seed-decorated barrels was determined as 88% (table S6) ($N = 129$). Note that no QDs were found attached to side surfaces of DNA barrels, confirming that QD attachment was specifically mediated by biotins as designed. After Ag growth, TEM imaging revealed the formation of QD-Ag-QD composite structures (31% casting yield; table S6) (Fig. 5B, right, and fig. S63) (29). Ag NPs exhibited a 20.5 ± 0.5 nm by 28.4 ± 1.3 nm projection ($N = 20$), consistent with the designed size of DNA barrel mold. Thus, we demonstrated the assembly of QD at prescribed locations on selected faces of a nonspherical metal NP.

Optimization of the casting process

The stoichiometry between anti-handle and Au seed was set to 1:1 to minimize the undesirable effect of surface-immobilized ssDNA on NP growth. To increase the formation yield of box-like DNA molds, we optimized the number of connectors on the barrels. Increasing the connectors from 6 to 14 at each end of the barrel increased the yield from less than 10% to 31%, whereas changing the lid-to-barrel ratio from 2:1 to 6:1 slightly raised the yield from 28% to 33%.

The effectiveness of the stiffness-based design strategy was verified by the following failed mold designs: Single-layered DNA mold did not produce pre-designed cross section shapes (fig. S67 and table S4); when the number of crossovers decreased to one or two, such as in the cases of DNA triangles that displayed sidewalls less than 16 nm thick, destructed DNA molds were observed during metal growth (figs. S69 and S71). We also note that although chemical inhibition between phosphate groups and the growing NP is also expected to occur (45, 46), it was not optimized as a design parameter for programming the shape in the current study. Additionally, the structural integrity of DNA molds was affected by the buffer ionic condition. At 10 mM magnesium nitrate, DNA mold remained intact for 1 day at 1 to 2 mM reactant concentration but deteriorated when the reactant concentration was higher than 20 mM. See (29) and figs. S66 to S75 for more details on the optimization of nanocasting and various suboptimal or failed DNA molds used in the optimization experiments.

Discussion

Previous work on casting NPs at a scale below 25 nm had only limited success, largely because of the lack of shape-programmable molds with both mechanical rigidity and surface programmability to enable site-specific seed decoration

followed by constrained growth. High-stiffness nanomolds such as viral capsids (35) and porous inorganic materials (47) are difficult to program into arbitrary geometric shapes, limiting their utility for nanoscale casting of diverse NP geometries and dimensions. Previous reports have shown the programming of 2D inorganic shapes with DNA templates. For example, the growth of metals mediated by randomly distributed nanocluster seeds (48–52) or strategically positioned NP seeds (53, 54) on a DNA nanostructure surface has produced diverse 2D shapes. However, rough surface morphologies (55) and inhomogeneous width distributions along the DNA skeletons (56) are often observed for these unconfined metalized products. Our work differs by providing a general way to construct inorganic nanostructures with arbitrarily user-specified 3D shapes and precise prescribed dimensions, by using DNA nanostructures to spatially confine the growth of the final shape (rather than seeding the initial shape) of the inorganic NP. The cast NP retains the addressable coating, whereas traditional chemical synthesis of surface-modified NPs typically involves multiple-step low-yield conjugation and purification after NP formation.

Rapid progress in DNA self-assembly will help to further expand the complexity and diversity of the NP shapes. Recent advances in scaffold-free 3D construction with DNA bricks have already demonstrated highly complex cavities (e.g., toroidal shape cavity) and tunnels (e.g., crossed and branched tunnels) encoded in sub-25-nm DNA cuboids (26). It is conceivable that such complex cavity and tunnel shapes may be transferred to inorganic substrates via DNA nanocasting. Further, because of the length limitation of the M13 viral scaffold strand, current multilayered mold designs using scaffolded DNA origami are restricted to producing sub-25-nm cavities. However, by using scaffold-free construction with DNA bricks (25, 26), DNA origami made from longer scaffolds (57), or hierarchical assembly of multiple origami (28, 58) and brick structures, nanomolds with much larger and more complex cavities may be achieved. In addition to increasing the shape complexity of the cast NPs, further research will also focus on expanding the material diversity of the NPs. Aside from Ag and Au, the Au seed can also mediate the growth of other diverse inorganic materials [e.g., metals (38, 39), oxides (40), and complex salts (41)] at mild conditions for potential casting with DNA molds. Replacing the Au seed with metal-binding peptides may further expand the cast diversity (e.g., metals, metal oxides, and chalcogenides) (59).

The casting yield (step 4) may be further optimized by using computer-aided design of DNA molds with high mechanical integrity to minimize mold distortion during growth. The formation of 3D enclosed, seed-decorated mold may be improved by optimizing self-assembly conditions [e.g., using isothermal folding (60)] or exploring alternative construction strategies [e.g., using DNA bricks (26)]. Additionally, replacing Au seeds (which tend to aggregate at DNA origami mold folding conditions) with more stable metal-

binding peptides could simplify the current multistep assembly strategy and enable one-step, high-yield formation of DNA molds with enclosed peptide seeds.

The shape- and surface-controlled inorganic NPs fabricated herein may eventually enable novel applications in diverse fields including biosensors, photonics, and nanoelectronics. Near-term applications are likely those based on single-particle properties. For example, DNA nanocasting produces a prescribed metal shape with a uniquely addressable coating, which may display the binding site for a target molecule at the near-field maximum position and hence enable highly sensitive detection. Because optical simulations of the cast NPs in water suggest geometry-specific dipolar resonances and near-field distributions (29), highly multiplexed sensing may be achieved using diverse programmed metal shapes.

DNA-based nanocasting represents a general approach for synthesizing inorganic nanostructures with arbitrarily prescribed 3D shapes (29). Together with other strategies for transferring the geometric information of DNA nanostructures to diverse inorganic materials [e.g., coating DNA nanostructures with inorganic oxides (61) or etching graphene using metalized DNA nanostructures as lithography masks (52)], it points to a new kind of manufacture framework: DNA-directed, digitally programmable fabrication of inorganic nanostructures and devices. Such DNA-based inorganic nanofabrication may eventually enable future production of sophisticated devices such as nanoscale optical circuits, electronic computers, and perhaps even inorganic molecular robots, each with their blueprints (or “genomes”) encoded in the DNA molecules that constitute their “nanofabricators.”

Materials and methods

DNA mold design

CaDNAno (30) was used to design the sequences and routing of staple strands using the scaffold strand (mutated P8064) derived from M13 bacteriophage.

Simulation of DNA mold mechanical properties

The mechanical properties of DNA molds were predicted using the finite-element method based on the ground-state 3D solution structure predicted by CanDo and standard geometric and mechanical properties of B-form DNA (31, 32). Mechanical deformations of the molds were computed in response to internal point and distributed loading using the commercial finite-element software ADINA (ADINA R&D Inc., Watertown, MA). Normal mode analysis was performed to compute the lowest-energy modes of deformation of the molds (29, 62, 63).

DNA mold folding

Assembly of DNA-origami molds was accomplished following previous reported protocols (22, 23). In a one-pot reaction, 50 nM scaffold was mixed with 250 nM staple strands (Bioneer Inc. or IDTDNA Inc.) in a buffer including 5 mM Tris,

1 mM EDTA, and 16 mM MgCl₂ (pH 8) and subjected to a thermal-annealing ramp that cooled from 80°C to 65°C over 75 min and then cooled from 64°C to 24°C over 70 hours.

Gel purification

We mixed 40 μl of folding products with 10 μl of glycerol, and the mixture was loaded into 1.5% agarose gel prestained with Sybr Safe containing 0.5× TBE and 10 mM Mg(NO₃)₂. The electrophoresis ran at 75 V for 3 hours in a gel box incubated in an ice-water bath. The monomer band was excised and origami was recovered by pestle crushing, followed by centrifugation for 3 min at 6000 rpm at room temperature using “Freeze ‘N Squeeze” DNA Gel Extraction spin columns (Bio-Rad). Recovered DNA molds were stored at 4°C for further use.

DNA decoration onto 5-nm Au seeds

Conjugation of thiolated DNA onto 5-nm Au seeds was achieved following previous reported protocol (64). In a typical experiment, 20 μl of 2.5 μM phosphine-coated 5-nm Au seeds were mixed with 0.5 μl of 2 M NaNO₃ and 0.65 μl of 100 μM thiolated DNA in 0.25× TBE buffer. The reaction solution was incubated at room temperature for 36 hours in the dark. After that, the reaction solution was loaded into 1% agarose gel containing 0.5× TBE buffer. The electrophoresis was running at 95 V for 1 hour in a gel box on an ice-water bath. The purple band was recovered by pestle crushing, followed by centrifugation for 3 min at 10,000 rpm at room temperature using “Freeze ‘N Squeeze” DNA Gel Extraction spin columns (Bio-Rad). Recovered DNA molds were stored at 4°C in dark for further use. The sequence for the thiolated DNA was TATGAGAAGTTAGGAATGTTATTTTT-Thiol. Note that thiol group was modified at the 3' end of anti-handle sequence TATGAGAAGTTAGGAATGTTA via a TTTTT spacer.

Seed decoration of DNA mold

Purified DNA molds were mixed with 50 mM NaNO₃ and 10 nM purified 5-nm Au-DNA conjugates (at a seed-to-barrel stoichiometry ratio of 2:1) and incubated at 35°C for 16 hours, followed by slow annealing to 24°C over 3 hours. The reaction buffer was then purified using an S300 spin column (GE Healthcare) by centrifugation for 2 min at 750g at room temperature to remove excessive Au-DNA conjugates.

Lid attachment onto DNA mold

DNA lids were mixed with the seed-decorated DNA barrels (at lid-to-barrel stoichiometry ratio of 3:1) at 35°C for 16 hours and annealed to 24°C over 3 hours.

Metal growth

For Ag growth, we added 0.5 μl of 14 mM AgNO₃ and 0.5 μl of 20 mM ascorbic acid to 5 μl of purified seed-decorated DNA molds at room temperature, and pipetted 30 times for mixing. Then the reaction solution was kept in the dark at room temperature for 4 to 20 min. For Au growth, 0.5 μl of 14 mM HAuCl₄ and 0.5 μl of 20 mM

ascorbic acid were added to 5 μl of purified seed-decorated DNA molds in 0.5× TB buffer at room temperature and pipetted 30 times for mixing. Then the reaction solution was kept in the dark at room temperature from 20 min to 2 hours.

TEM

NPs (3.5 μl) were adsorbed onto glow-discharged carbon-coated TEM grids for 2 min and then wiped away, followed by staining with 3.5 μl of 2% aqueous uranyl formate solution containing 25 mM NaOH for 45 s. Imaging was performed using a JEOL 1400 operated at 80 kV. High-resolution TEM and electron diffraction were performed using a JEOL 2010 with FEG operated at 200 kV for unstained NP sample deposited onto amorphous carbon film.

Yield analysis

Seed decoration yield from step 2, box closure yield from step 3, and casting yield from step 4 (29) in Fig. 1A were acquired through direct counting of NPs with prescribed shapes and dimensions from each of the three projection views. For each individual barrel and lid, the barrel and the lid formation yield from step 1a (Fig. 1A) were determined from agarose gel (29).

EELS experimental characterization

The low-loss EELS data were collected with TEAM I at the Lawrence Berkeley National Lab, a monochromated TEM operated at 80 kV. The EELS data were collected in the TEM mode under vacuum for the unstained NP sample deposited onto amorphous carbon film.

Simulation of NP plasmonic and optical properties

EELS results were simulated using MNPBEM (65, 66), which is freely available as a MATLAB (MathWorks Inc., Natick, MA) toolbox (29). Optical property simulations were performed using the commercial finite element software COMSOL (COMSOL Inc., Burlington, MA) employing the full 3D continuum electromagnetic Helmholtz equation (29, 67, 68).

REFERENCES AND NOTES

- P. P. Pompa *et al.*, Metal-enhanced fluorescence of colloidal nanocrystals with nanoscale control. *Nat. Nanotechnol.* **1**, 126–130 (2006). doi: [10.1038/nnano.2006.93](https://doi.org/10.1038/nnano.2006.93); pmid: [18654164](https://pubmed.ncbi.nlm.nih.gov/18654164/)
- F. Wang *et al.*, Plasmonic harvesting of light energy for Suzuki coupling reactions. *J. Am. Chem. Soc.* **135**, 5588–5601 (2013). doi: [10.1021/ja310501y](https://doi.org/10.1021/ja310501y); pmid: [23521598](https://pubmed.ncbi.nlm.nih.gov/23521598/)
- A. V. Kildishev, A. Boltasseva, V. M. Shalaev, Planar photonics with metasurfaces. *Science* **339**, 1232009 (2013). doi: [10.1126/science.1232009](https://doi.org/10.1126/science.1232009); pmid: [23493714](https://pubmed.ncbi.nlm.nih.gov/23493714/)
- A. L. Koh, A. I. Fernández-Domínguez, D. W. McComb, S. A. Maier, J. K. W. Yang, High-resolution mapping of electron-beam-excited plasmon modes in lithographically defined gold nanostructures. *Nano Lett.* **11**, 1323–1330 (2011). doi: [10.1021/nl104410t](https://doi.org/10.1021/nl104410t); pmid: [21344928](https://pubmed.ncbi.nlm.nih.gov/21344928/)
- Y. Sun, Y. Xia, Shape-controlled synthesis of gold and silver nanoparticles. *Science* **298**, 2176–2179 (2002). doi: [10.1126/science.1077229](https://doi.org/10.1126/science.1077229); pmid: [12481134](https://pubmed.ncbi.nlm.nih.gov/12481134/)
- Y. Xia, Y. Xiong, B. Lim, S. E. Skrabalak, Shape-controlled synthesis of metal nanocrystals: Simple chemistry meets complex physics? *Angew. Chem. Int. Ed.* **48**, 60–103 (2009). doi: [10.1002/anie.200802248](https://doi.org/10.1002/anie.200802248); pmid: [19053095](https://pubmed.ncbi.nlm.nih.gov/19053095/)
- T. Ming *et al.*, Growth of tetrahedral gold nanocrystals with high-index facets. *J. Am. Chem. Soc.* **131**, 16350–16351 (2009). doi: [10.1021/ja907549n](https://doi.org/10.1021/ja907549n); pmid: [19856912](https://pubmed.ncbi.nlm.nih.gov/19856912/)

- N. Ma, E. H. Sargent, S. O. Kelley, One-step DNA-programmed growth of luminescent and biofunctionalized nanocrystals. *Nat. Nanotechnol.* **4**, 121–125 (2009). doi: [10.1038/nnano.2008.373](https://doi.org/10.1038/nnano.2008.373); pmid: [19197315](https://pubmed.ncbi.nlm.nih.gov/19197315/)
- S. E. Lohse, C. J. Murphy, Applications of colloidal inorganic nanoparticles: From medicine to energy. *J. Am. Chem. Soc.* **134**, 15607–15620 (2012). doi: [10.1021/ja307589n](https://doi.org/10.1021/ja307589n); pmid: [22934680](https://pubmed.ncbi.nlm.nih.gov/22934680/)
- Z. Wang, L. Tang, L. H. Tan, J. Li, Y. Lu, Discovery of the DNA “genetic code” for abiological gold nanoparticle morphologies. *Angew. Chem. Int. Ed.* **51**, 9078–9082 (2012). doi: [10.1002/anie.201203716](https://doi.org/10.1002/anie.201203716); pmid: [22865657](https://pubmed.ncbi.nlm.nih.gov/22865657/)
- L. Ruan *et al.*, Tailoring molecular specificity toward a crystal facet: A lesson from biorecognition toward Pt(111). *Nano Lett.* **13**, 840–846 (2013). doi: [10.1021/nl400022g](https://doi.org/10.1021/nl400022g); pmid: [23320831](https://pubmed.ncbi.nlm.nih.gov/23320831/)
- A. Puzder *et al.*, The effect of organic ligand binding on the growth of CdSe nanoparticles probed by ab initio calculations. *Nano Lett.* **4**, 2361–2365 (2004). doi: [10.1021/nl0485861](https://doi.org/10.1021/nl0485861)
- J. Yu, M. L. Becker, G. A. Carri, A molecular dynamics simulation of the stability-limited growth mechanism of peptide-mediated gold-nanoparticle synthesis. *Small* **6**, 2242–2245 (2010). doi: [10.1002/smll.201000889](https://doi.org/10.1002/smll.201000889); pmid: [20853372](https://pubmed.ncbi.nlm.nih.gov/20853372/)
- C. R. Bealing, W. J. Baumgardner, J. J. Choi, T. Hanrath, R. G. Hennig, Predicting nanocrystal shape through consideration of surface-ligand interactions. *ACS Nano* **6**, 2118–2127 (2012). doi: [10.1021/nn3000466](https://doi.org/10.1021/nn3000466); pmid: [22329695](https://pubmed.ncbi.nlm.nih.gov/22329695/)
- N. C. Seeman, DNA in a material world. *Nature* **421**, 427–431 (2003). doi: [10.1038/nature04106](https://doi.org/10.1038/nature04106); pmid: [12540916](https://pubmed.ncbi.nlm.nih.gov/12540916/)
- J. H. Chen, N. C. Seeman, Synthesis from DNA of a molecule with the connectivity of a cube. *Nature* **350**, 631–633 (1991). doi: [10.1038/350631a0](https://doi.org/10.1038/350631a0); pmid: [2017259](https://pubmed.ncbi.nlm.nih.gov/2017259/)
- E. Winfree, F. Liu, L. A. Wenzler, N. C. Seeman, Design and self-assembly of two-dimensional DNA crystals. *Nature* **394**, 539–544 (1998). doi: [10.1038/28998](https://doi.org/10.1038/28998); pmid: [9707114](https://pubmed.ncbi.nlm.nih.gov/9707114/)
- W. M. Shih, J. D. Quispe, G. F. Joyce, A 1.7-kilobase single-stranded DNA that folds into a nanoscale octahedron. *Nature* **427**, 618–621 (2004). doi: [10.1038/nature02307](https://doi.org/10.1038/nature02307); pmid: [14961116](https://pubmed.ncbi.nlm.nih.gov/14961116/)
- P. W. K. Rothmund, Folding DNA to create nanoscale shapes and patterns. *Nature* **440**, 297–302 (2006). doi: [10.1038/nature04586](https://doi.org/10.1038/nature04586); pmid: [16541064](https://pubmed.ncbi.nlm.nih.gov/16541064/)
- P. Yin *et al.*, Programming DNA tube circumferences. *Science* **321**, 824–826 (2008). doi: [10.1126/science.1157312](https://doi.org/10.1126/science.1157312); pmid: [18687961](https://pubmed.ncbi.nlm.nih.gov/18687961/)
- Y. He *et al.*, Hierarchical self-assembly of DNA into symmetric supramolecular polyhedra. *Nature* **452**, 198–201 (2008). doi: [10.1038/nature06597](https://doi.org/10.1038/nature06597); pmid: [18337818](https://pubmed.ncbi.nlm.nih.gov/18337818/)
- S. M. Douglas *et al.*, Self-assembly of DNA into nanoscale three-dimensional shapes. *Nature* **459**, 414–418 (2009). doi: [10.1038/nature08016](https://doi.org/10.1038/nature08016); pmid: [19458720](https://pubmed.ncbi.nlm.nih.gov/19458720/)
- H. Dietz, S. M. Douglas, W. M. Shih, Folding DNA into twisted and curved nanoscale shapes. *Science* **325**, 725–730 (2009). doi: [10.1126/science.1174251](https://doi.org/10.1126/science.1174251); pmid: [19661424](https://pubmed.ncbi.nlm.nih.gov/19661424/)
- D. Han *et al.*, DNA origami with complex curvatures in three-dimensional space. *Science* **332**, 342–346 (2011). doi: [10.1126/science.1202998](https://doi.org/10.1126/science.1202998); pmid: [21493857](https://pubmed.ncbi.nlm.nih.gov/21493857/)
- B. Wei, M. Dai, P. Yin, Complex shapes self-assembled from single-stranded DNA tiles. *Nature* **485**, 623–626 (2012). doi: [10.1038/nature11075](https://doi.org/10.1038/nature11075); pmid: [22660323](https://pubmed.ncbi.nlm.nih.gov/22660323/)
- Y. Ke, L. L. Ong, W. M. Shih, P. Yin, Three-dimensional structures self-assembled from DNA bricks. *Science* **338**, 1177–1183 (2012). doi: [10.1126/science.1227268](https://doi.org/10.1126/science.1227268); pmid: [23197527](https://pubmed.ncbi.nlm.nih.gov/23197527/)
- D. Han *et al.*, DNA gridiron nanostructures based on four-arm junctions. *Science* **339**, 1412–1415 (2013). doi: [10.1126/science.1232252](https://doi.org/10.1126/science.1232252); pmid: [23520107](https://pubmed.ncbi.nlm.nih.gov/23520107/)
- R. Iinuma *et al.*, Polyhedra self-assembled from DNA tripods and characterized with 3D DNA-PAINT. *Science* **344**, 65–69 (2014). doi: [10.1126/science.1250944](https://doi.org/10.1126/science.1250944); pmid: [24625926](https://pubmed.ncbi.nlm.nih.gov/24625926/)
- See supplementary materials on Science Online.
- S. M. Douglas *et al.*, Rapid prototyping of three-dimensional DNA-origami shapes with caDNA. *Nucleic Acids Res.* **37**, 5001–5006 (2009). doi: [10.1093/nar/gkp436](https://doi.org/10.1093/nar/gkp436); pmid: [19531737](https://pubmed.ncbi.nlm.nih.gov/19531737/)
- C. E. Castro *et al.*, A primer to scaffolded DNA origami. *Nat. Methods* **8**, 221–229 (2011). doi: [10.1038/nmeth.1570](https://doi.org/10.1038/nmeth.1570); pmid: [21358626](https://pubmed.ncbi.nlm.nih.gov/21358626/)
- D. N. Kim, F. Kilchherr, H. Dietz, M. Bathe, Quantitative prediction of 3D solution shape and flexibility of nucleic acid nanostructures. *Nucleic Acids Res.* **40**, 2862–2868 (2012). doi: [10.1093/nar/gkr1173](https://doi.org/10.1093/nar/gkr1173); pmid: [22156372](https://pubmed.ncbi.nlm.nih.gov/22156372/)
- Y. Ke *et al.*, Multilayer DNA origami packed on a square lattice. *J. Am. Chem. Soc.* **131**, 15903–15908 (2009). doi: [10.1021/ja906381y](https://doi.org/10.1021/ja906381y); pmid: [19807088](https://pubmed.ncbi.nlm.nih.gov/19807088/)

34. J. P. Michel *et al.*, Nanoindentation studies of full and empty viral capsids and the effects of capsid protein mutations on elasticity and strength. *Proc. Natl. Acad. Sci. U.S.A.* **103**, 6184–6189 (2006). doi: [10.1073/pnas.0601744103](https://doi.org/10.1073/pnas.0601744103); pmid: [16606825](https://pubmed.ncbi.nlm.nih.gov/16606825/)
35. M. B. Dickerson, K. H. Sandhage, R. R. Naik, Protein- and peptide-directed syntheses of inorganic materials. *Chem. Rev.* **108**, 4935–4978 (2008). doi: [10.1021/cr800232z](https://doi.org/10.1021/cr800232z); pmid: [18973389](https://pubmed.ncbi.nlm.nih.gov/18973389/)
36. Z. Zhao, E. L. Jacovetty, Y. Liu, H. Yan, Encapsulation of gold nanoparticles in a DNA origami cage. *Angew. Chem. Int. Ed.* **50**, 2041–2044 (2011). doi: [10.1002/anie.201006818](https://doi.org/10.1002/anie.201006818); pmid: [21344547](https://pubmed.ncbi.nlm.nih.gov/21344547/)
37. D. Zanchet, C. M. Micheel, W. J. Parak, D. Gerion, A. P. Alivisatos, Electrophoretic isolation of discrete Au nanocrystal/DNA conjugates. *Nano Lett.* **1**, 32–35 (2001). doi: [10.1021/nl005508e](https://doi.org/10.1021/nl005508e)
38. F. R. Fan *et al.*, Epitaxial growth of heterogeneous metal nanocrystals: From gold nano-octahedra to palladium and silver nanocubes. *J. Am. Chem. Soc.* **130**, 6949–6951 (2008). doi: [10.1021/ja801566d](https://doi.org/10.1021/ja801566d); pmid: [18465860](https://pubmed.ncbi.nlm.nih.gov/18465860/)
39. F. Wang *et al.*, Heteroepitaxial growth of high-index-faceted palladium nanoshells and their catalytic performance. *J. Am. Chem. Soc.* **133**, 1106–1111 (2011). doi: [10.1021/ja109573z](https://doi.org/10.1021/ja109573z); pmid: [21174411](https://pubmed.ncbi.nlm.nih.gov/21174411/)
40. R. G. Chaudhuri, S. Paria, Core/shell nanoparticles: Classes, properties, synthesis mechanisms, characterization, and applications. *Chem. Rev.* **112**, 2373–2433 (2012). doi: [10.1021/cr100449n](https://doi.org/10.1021/cr100449n); pmid: [22204603](https://pubmed.ncbi.nlm.nih.gov/22204603/)
41. G. Maurin-Pasturel *et al.*, Nanosized heterostructures of Au@ Prussian blue analogues: Towards multifunctionality at the nanoscale. *Angew. Chem. Int. Ed.* **53**, 3872–3876 (2014). doi: [10.1002/anie.201310443](https://doi.org/10.1002/anie.201310443); pmid: [24574155](https://pubmed.ncbi.nlm.nih.gov/24574155/)
42. J. A. Scholl, A. L. Koh, J. A. Dionne, Quantum plasmon resonances of individual metallic nanoparticles. *Nature* **483**, 421–427 (2012). doi: [10.1038/nature09094](https://doi.org/10.1038/nature09094); pmid: [22437611](https://pubmed.ncbi.nlm.nih.gov/22437611/)
43. J. Nelayah *et al.*, Mapping surface plasmons on a single metallic nanoparticle. *Nat. Phys.* **3**, 348–353 (2007). doi: [10.1038/nphys575](https://doi.org/10.1038/nphys575)
44. V. Myroshnychenko *et al.*, Plasmon spectroscopy and imaging of individual gold nanodecahedra: A combined optical microscopy, cathodoluminescence, and electron energy-loss spectroscopy study. *Nano Lett.* **12**, 4172–4180 (2012). doi: [10.1021/nl301742h](https://doi.org/10.1021/nl301742h); pmid: [22746278](https://pubmed.ncbi.nlm.nih.gov/22746278/)
45. L. Berti, G. A. Burley, Nucleic acid and nucleotide-mediated synthesis of inorganic nanoparticles. *Nat. Nanotechnol.* **3**, 81–87 (2008). doi: [10.1038/nnano.2007.460](https://doi.org/10.1038/nnano.2007.460); pmid: [18654466](https://pubmed.ncbi.nlm.nih.gov/18654466/)
46. S. J. Tan, M. J. Campolongo, D. Luo, W. Cheng, Building plasmonic nanostructures with DNA. *Nat. Nanotechnol.* **6**, 268–276 (2011). doi: [10.1038/nnano.2011.49](https://doi.org/10.1038/nnano.2011.49); pmid: [21499251](https://pubmed.ncbi.nlm.nih.gov/21499251/)
47. C. Gao, Q. Zhang, Z. Lu, Y. Yin, Templated synthesis of metal nanorods in silica nanotubes. *J. Am. Chem. Soc.* **133**, 19706–19709 (2011). doi: [10.1021/ja209647d](https://doi.org/10.1021/ja209647d); pmid: [22085084](https://pubmed.ncbi.nlm.nih.gov/22085084/)
48. E. Braun, Y. Eichen, U. Sivan, G. Ben-Yoseph, DNA-templated assembly and electrode attachment of a conducting silver wire. *Nature* **391**, 775–778 (1998). doi: [10.1038/35826](https://doi.org/10.1038/35826); pmid: [9486645](https://pubmed.ncbi.nlm.nih.gov/9486645/)
49. H. Yan, S. H. Park, G. Finkelstein, J. H. Reif, T. H. LaBean, DNA-templated self-assembly of protein arrays and highly conductive nanowires. *Science* **301**, 1882–1884 (2003). doi: [10.1126/science.1089389](https://doi.org/10.1126/science.1089389); pmid: [14512621](https://pubmed.ncbi.nlm.nih.gov/14512621/)
50. J. Liu *et al.*, Metallization of branched DNA origami for nanoelectronic circuit fabrication. *ACS Nano* **5**, 2240–2247 (2011). doi: [10.1021/nn1035075](https://doi.org/10.1021/nn1035075); pmid: [21323323](https://pubmed.ncbi.nlm.nih.gov/21323323/)
51. R. Schreiber *et al.*, DNA origami-templated growth of arbitrarily shaped metal nanoparticles. *Small* **7**, 1795–1799 (2011). doi: [10.1002/sml.201100465](https://doi.org/10.1002/sml.201100465); pmid: [21608127](https://pubmed.ncbi.nlm.nih.gov/21608127/)
52. Z. Jin *et al.*, Metallized DNA nanolithography for encoding and transferring spatial information for graphene patterning. *Nat. Commun.* **4**, 1663 (2013). doi: [10.1038/ncomms2690](https://doi.org/10.1038/ncomms2690); pmid: [23575667](https://pubmed.ncbi.nlm.nih.gov/23575667/)
53. M. Pilo-Pais, S. Goldberg, E. Samano, T. H. Labeau, G. Finkelstein, Connecting the nanodots: Programmable nanofabrication of fused metal shapes on DNA templates. *Nano Lett.* **11**, 3489–3492 (2011). doi: [10.1021/nl202066c](https://doi.org/10.1021/nl202066c); pmid: [21732612](https://pubmed.ncbi.nlm.nih.gov/21732612/)
54. A. Kuzyk *et al.*, DNA-based self-assembly of chiral plasmonic nanostructures with tailored optical response. *Nature* **483**, 311–314 (2012). doi: [10.1038/nature10889](https://doi.org/10.1038/nature10889); pmid: [22422265](https://pubmed.ncbi.nlm.nih.gov/22422265/)
55. E. C. Samano *et al.*, Self-assembling DNA templates for programmed artificial biomineralization. *Soft Matter* **7**, 3240–3245 (2011). doi: [10.1039/c0sm01318h](https://doi.org/10.1039/c0sm01318h)
56. M. Fischler *et al.*, Formation of bimetallic Ag-Au nanowires by metallization of artificial DNA duplexes. *Small* **3**, 1049–1055 (2007). doi: [10.1002/sml.200600534](https://doi.org/10.1002/sml.200600534); pmid: [17309092](https://pubmed.ncbi.nlm.nih.gov/17309092/)
57. H. Zhang *et al.*, Folding super-sized DNA origami with scaffold strands from long-range PCR. *Chem. Commun.* **48**, 6405–6407 (2012). doi: [10.1039/c2cc32204h](https://doi.org/10.1039/c2cc32204h); pmid: [22618197](https://pubmed.ncbi.nlm.nih.gov/22618197/)
58. S. Woo, P. W. K. Rothmund, Programmable molecular recognition based on the geometry of DNA nanostructures. *Nat. Chem.* **3**, 620–627 (2011). doi: [10.1038/nchem.1070](https://doi.org/10.1038/nchem.1070); pmid: [21778982](https://pubmed.ncbi.nlm.nih.gov/21778982/)
59. M. Sarikaya, C. Tamerler, A. K. Y. Jen, K. Schulten, F. Baneyx, Molecular biomimetics: Nanotechnology through biology. *Nat. Mater.* **2**, 577–585 (2003). doi: [10.1038/nmat964](https://doi.org/10.1038/nmat964); pmid: [12951599](https://pubmed.ncbi.nlm.nih.gov/12951599/)
60. J.-P. J. Sobczak, T. G. Martin, T. Gerling, H. Dietz, Rapid folding of DNA into nanoscale shapes at constant temperature. *Science* **338**, 1458–1461 (2012). doi: [10.1126/science.1229919](https://doi.org/10.1126/science.1229919); pmid: [23239734](https://pubmed.ncbi.nlm.nih.gov/23239734/)
61. S. P. Surwade *et al.*, Nanoscale growth and patterning of inorganic oxides using DNA nanostructure templates. *J. Am. Chem. Soc.* **135**, 6778–6781 (2013). doi: [10.1021/ja401785h](https://doi.org/10.1021/ja401785h); pmid: [23574340](https://pubmed.ncbi.nlm.nih.gov/23574340/)
62. M. Bathe, A finite element framework for computation of protein normal modes and mechanical response. *Proteins* **70**, 1595–1609 (2008). doi: [10.1002/prot.21708](https://doi.org/10.1002/prot.21708); pmid: [17975833](https://pubmed.ncbi.nlm.nih.gov/17975833/)
63. B. Brooks, D. Janežič, M. Karplus, Harmonic analysis of large systems. I. methodology. *J. Comput. Chem.* **16**, 1522–1542 (1995). doi: [10.1002/jcc.540161209](https://doi.org/10.1002/jcc.540161209)
64. J. Sharma *et al.*, Toward reliable gold nanoparticle patterning on self-assembled DNA nanoscaffold. *J. Am. Chem. Soc.* **130**, 7820–7821 (2008). doi: [10.1021/ja802853r](https://doi.org/10.1021/ja802853r); pmid: [18510317](https://pubmed.ncbi.nlm.nih.gov/18510317/)
65. U. Hohenester, A. Trügler, MNPBEM a matlab toolbox for the simulation of plasmonic nanoparticles. *Comput. Phys. Commun.* **183**, 370–381 (2012). doi: [10.1016/j.cpc.2011.09.009](https://doi.org/10.1016/j.cpc.2011.09.009)
66. U. Hohenester, Simulating electron energy loss spectroscopy with the MNPBEM toolbox. *Comput. Phys. Commun.* **185**, 1177–1187 (2014). doi: [10.1016/j.cpc.2013.12.010](https://doi.org/10.1016/j.cpc.2013.12.010)
67. E. Boulais, R. Lachaine, M. Meunier, Plasma mediated off-resonance plasmonic enhanced ultrafast laser-induced nanocavitation. *Nano Lett.* **12**, 4763–4769 (2012). doi: [10.1021/nl302200w](https://doi.org/10.1021/nl302200w); pmid: [22845691](https://pubmed.ncbi.nlm.nih.gov/22845691/)
68. E. Boulais, R. Lachaine, M. Meunier, Plasma-mediated nanocavitation and photothermal effects in ultrafast laser irradiation of gold nanorods in water. *J. Phys. Chem. C* **117**, 9386–9396 (2013). doi: [10.1021/jp312475h](https://doi.org/10.1021/jp312475h)

ACKNOWLEDGMENTS

We thank Y. Ke, J. Shen, and B. Wei for discussion, and E. Haney, D. Pastuszak and E. Chen for assistance in draft preparation. Supported by Defense Advanced Research Projects Agency Young Faculty Award N6600111413, Office of Naval Research (ONR) Young Investigator Program Award N00014110914, ONR grants N000141010827, N000141310593, and N000141410610, Army Research Office grant W911NF1210238, NIH Director's New Innovator Award 1DP2OD007292, NSF Faculty Early Career Development Award CCF1054898, NSF Expedition in Computing Award CCF1317291, NSF grants CCF1162459, CMMI1333215, CMMI1334109, and CMMI1344915 and Wyss Institute funds (P.Y.); ONR grants DURIP N000141310664 and N000141210621 and NSF-DMREF grant CMMI1334109 (M.B., E.B., and Y.H.); and the Natural Sciences and Engineering Research Council of Canada (E.B.). This work was performed in part at the Center for Nanoscale Systems (CNS), a member of the National Nanotechnology Infrastructure Network (NNIN), which is supported by NSF award ECS-0335765. CNS is part of Harvard University. The EELS of the Ag NPs was measured at National Center for Electron Microscopy, which is supported by the Office of Science, Office of Basic Energy Sciences, U.S. Department of Energy under contract DE-AC0205CH11231. Contributions: W.S. designed the system, conducted the experiments, and analyzed the data; E.B. designed and performed optical and EELS simulations, and analyzed the data; Y.H. designed and performed mechanical simulation, and analyzed the data; W.L.W. performed EELS experiments and analyzed the data; A.G. performed experiments and analyzed the data; M.B. designed and supervised the simulation study and interpreted the data; P.Y. conceived, designed, and supervised the study and interpreted the data; and all authors wrote the manuscript. All data described in this article are presented in the supplementary materials.

SUPPLEMENTARY MATERIALS

www.sciencemag.org/content/346/6210/1258361/suppl/DC1
Materials and Methods
Supplementary Text
Figs. S1 to S75
Tables S1 to S6
References (69–84)

7 July 2014; accepted 30 September 2014
Published online 9 October 2014;
[10.1126/science.1258361](https://doi.org/10.1126/science.1258361)

This copy is for your personal, non-commercial use only.

If you wish to distribute this article to others, you can order high-quality copies for your colleagues, clients, or customers by [clicking here](#).

Permission to republish or repurpose articles or portions of articles can be obtained by following the guidelines [here](#).

The following resources related to this article are available online at www.sciencemag.org (this information is current as of February 9, 2015):

Updated information and services, including high-resolution figures, can be found in the online version of this article at:

<http://www.sciencemag.org/content/346/6210/1258361.full.html>

Supporting Online Material can be found at:

<http://www.sciencemag.org/content/suppl/2014/10/08/science.1258361.DC1.html>

This article **cites 81 articles**, 14 of which can be accessed free:

<http://www.sciencemag.org/content/346/6210/1258361.full.html#ref-list-1>

This article appears in the following **subject collections**:

Materials Science

http://www.sciencemag.org/cgi/collection/mat_sci